Control of Wigner localization and electron cavity effects in near-field emission spectra of In(Ga)P/GaInP quantum-dot structures

A. M. Mintairov,[1,2,*] J. Kapaldo,[1] J. L. Merz,[1] S. Rouvimov,[1] D. V. Lebedev,[2] N. A. Kalyuzhnyy,[2] S. A. Mintairov,[2] K. G. Belyaev,[2] M. V. Rakhlin,[2] A. A. Toropov,[2] P. N. Brunkov,[2] A. S. Vlasov,[2] Yu. M. Zadiranov,[2] S. A. Blundell,[3] A. M. Mozharov,[4] I. Mukhin,[4] M. Yakimov,[5] S. Oktyabrsky,[5] A. V. Shelaev,[6] and V. A. Bykov[6]
[1]*University of Notre Dame, Notre Dame, Indiana 46556, USA*
[2]*Ioffe Physical-Technical Institute of the Russian Academy of Sciences, Saint Petersburg 194021, Russia*
[3]*University Grenoble Alpes, CEA, Centre National de la Recherche Scientifique, INAC, SyMMES, F-38000 Grenoble, France*
[4]*Saint Petersburg Academic University, 194021 Saint Petersburg, Russia*
[5]*SUNY, Albany, New York 12222, USA*
[6]*NT-MDT, Co., Zelenograd, Moscow 124460, Russia*

(Received 6 March 2018; revised manuscript received 26 April 2018; published 29 May 2018)

Structural and emission properties of few-electron In(Ga)P/GaInP quantum dots (QDs) representing natural Wigner molecules (WM) and whispering gallery mode (WGM) electron (e) cavities have been investigated. QD structures were grown using self-organized metal-organic vapor phase epitaxy and deposition from ~3 to 7 monolayers of InP at 700 °C. Using atomic force microscopy, transmission electron microscopy, near-field scanning optical microscopy (NSOM), and μ-photoluminescence (μ-PL) spectra we obtained In(Ga)P/GaInP QDs having lateral size 80–180 nm, height 5–30 nm, Ga content 0.0–0.4, density $2-10\,\mu\mathrm{m}^{-2}$, and electron population up to 20 and demonstrated control of their density and size distribution. Using high-spatial-resolution low-temperature PL spectra, NSOM imaging, and calculations of charge density distributions we observed Wigner localization and e-cavity effects for a series of dots having quantum confinement $\hbar\omega_0 = 0.5-6\,\mathrm{meV}$. We used these data together with time-resolved PL measurements to clarify the effect of Coulomb interaction and WM formation on emission spectra of few-electron QDs. We present direct observation of 2e, 6e, and 9e WMs; 2e and 4e WGMs; and Fabry-Perot e modes and establish conditions of e-WGM-cavity formation in these QDs.

DOI: 10.1103/PhysRevB.97.195443

I. INTRODUCTION

Semiconductor quantum dots (QDs) containing only a few electrons represent two-dimensional (2D) manmade analogs of atoms and resemble shell structure and periodic table behavior, Hund's rule, and spin singlet and triplet states [1,2] similar to that of atomic physics in three dimensions. Having a few orders of magnitude larger size and smaller quantization energy than natural atoms, these "artificial" atoms represent a quantum system, in which the electron-electron interaction energy becomes comparable to the kinetic energy, and which gives rise to specific phenomena such as Wigner localization (WL) [3–6] and the formation of strongly correlated quantum states induced by a high magnetic field [7–9]. These quantum states are expected to be similar to those observed in the quantum Hall effect [10] and are interesting for realization of topological quantum computing, using localized non-Abelian anyons [11]. Also, due to quantum confinement, QDs can be used for the formation of electron whispering gallery mode (WGM) resonators [12], as recently claimed in molecular nanoring [13] and graphene nanodisk [14] structures. This opens up a new field of solid state integrated "electron optics."

A key artificial atom system commonly used is that of Ga(In)As/AlGaAs QDs formed from planar quantum well (QW) structures using nanofabrication techniques; atomiclike behavior for these dots was demonstrated a few decades ago using charge transport measurements and electrostatic gates [1]. In general, these dots provide virtually full control of individual electrons and, in particular, demonstrate the manipulation of spins in dots containing one and two electrons, which is relevant for single-spin-related quantum information processing and spintronics [2]. However, they show relatively weak electron correlation effects [3–6] due to the intrinsic inhomogeneity of QW material [15], nanofabrication defects [16], and soft-wall confined potentials [17]; these limit their implementation in topological quantum processing, intrinsically involving many-particle interactions. Also for these dots no WGM resonator has been reported.

A different few-electron 2D QD system, which revealed stronger electron correlation and can be more useful for topological quantum computing, is a system based on self-organized InP/GaInP QD structures [18]. These structures are being grown by metal-organic vapor phase epitaxy (MOVPE) using deposition of ~7 monolayers (ML) of InP and provide QDs having bimodal height distribution with peaks at ~5 and ~15 nm, lateral size ~160 nm, Ga content up to 20%, and density ~$20\,\mu\mathrm{m}^{-2}$ [18]. Substantial Ga content, induced by a Ga-In intermixing effect [18], allows us to denote these QDs as In(Ga)P/GaInP QDs, instead of InP/GaInP QDs used by us in previous studies [12,19], and we will use the former notation further.

---

[*] Corresponding author: amintair@nd.edu

TABLE I. Parameters of In(Ga)P/GaInP QD structures.

					H (nm)			Density (μm^{-2})			
No.		d_{InP} (nm)	d_{cap} (nm)	D (nm)	A	B	C	A	B	C	Measurement technique
1	AIX568a	7	0	150	5	13-21	30	15	6.5	1.5	AFM
2	AIX2383	4.5	0	200	4	12-9		4	4		AFM
3	AIX2012	2.9	0	180	3-6	10		10	0.8		AFM
4	X3141[a]	7	60	~150		10			20		TEM, NSOM
5	AIX817	7	40	140	5	10/20	30	8	8	2	TEM, NSOM
6	AIX2421	3	40	130/170	5	10		9	1		TEM, μ-PL

[a]TEM data were taken from [22].

An unusual and interesting feature of these dots observed by us [18,19] is a rich emission structure of photoluminescence (PL) spectra revealing transitions related to occupied electronic shells and relative-motion excitations of the electrons, which provides efficient contactless control of electron occupation, shell energy splitting, and electron arrangement. This allows us to use PL spectra to demonstrate that In(Ga)P/GaInP QDs dots have quantum confinement as low as $\hbar\omega_0 \sim 0.5$ meV and electron population up to $N \sim 20$ *in situ* and they could represent natural Wigner molecules (WMs) [18,19]. Also we have shown that due to the hard-wall edge potential these QDs can be used as WGM resonators [12]. Further investigations of WL and cavity effects in this QD system are needed for clarifying their possible applications.

In the present paper we report growth experiments and structural and high-spatial-resolution PL spectroscopy measurements of In(Ga)P/GaInP QD structures which demonstrate *in situ* control of dot density and WL/WGM-cavity effects, which is based on the control of dot height and Ga-In intermixing. In the growth experiments we used MOVPE and variation of the InP thickness from 7 to 3 ML in Stransky-Krastanov growth mode together with atomic force and transmission microscopy measurements. We measured emission spectra of nearly 120 individual QDs in the samples having dot density from 1 to 20 μm^{-2} using μ-PL and near-field scanning optical microscopy (NSOM) techniques. In the paper presented here we show the measurements of the spectral, spatial, and temporal distribution of the emission intensity of a selected set of 22 dots having $N = 1-9$ and quantum confinement in the range $\hbar\omega_0 = 0.5-6$ meV together with the calculations of their charged density distributions. We use these to clarify effects of the Coulomb interaction and a formation of WMs on the emission structure and NSOM images of strongly correlated confined electrons. We demonstrate direct observation of the $2e$, $6e$, and $9e$ WMs; $2e$ and $4e$ WGMs; and Fabry-Perot e modes and find the conditions of their formation.

II. EXPERIMENTAL DETAILS AND SAMPLES

The MOVPE growth procedure and the various microscopy techniques used, such as atomic force microscopy (AFM), transmission electron microscopy (TEM), μ-PL, and low-temperature optical-fiber-based NSOM techniques, have all been described earlier [18]. In addition, a room-temperature NSOM utilizing cantilevered probes and time-resolved PL techniques, described in [20] and [21], respectively, has been used.

We used AFM to measure dot diameter (D) and height (H) and their probability density functions (PDFs) for the uncapped samples. We used TEM and PL/NSOM to measure $D(H)$ and emission spectra, respectively, of QDs in the capped sample.

Here we present data for three uncapped samples ($d_{\mathrm{cap}} = 0$ nm) having InP thickness $d_{\mathrm{InP}} = 2.9, 4.5,$ and 7 ML and three capped samples—two having $d_{\mathrm{InP}} =$ 7 ML ($d_{\mathrm{cap}} = 60$ and 40 nm) and one having $d_{\mathrm{InP}} = 3$ ML ($d_{\mathrm{cap}} = 40$ nm). A few more uncapped samples, having d_{InP} down to 2 ML, and capped samples having d_{cap} down to 5 nm have been also measured in a preliminary study.

The uncapped and capped samples are denoted as 1, 2, and 3 and 4, 5, and 6, respectively, and their parameters measured are presented in Table I. For sample 4 we used TEM data from [22].

In sample 6 (3 ML capped) we etched arrays of 500-nm diameter mesas using electron-beam lithography and we used μ-PL to measure emission spectra and decay time of nearly 20 single dots located in individual mesas. We found that measured emission decay curves can be fitted using two exponents, having characteristic decay times $\tau_0 = 0.35-0.8$ ns and $\tau_1 = 80-100$ ns. We did not observe the τ_1 component in our previous study [18] and will not discuss it below.

Nearly 100 individual dots have been measured using NSOM of 7-ML samples 4 and 5. NSOM images of six QDs have been already reported [18,19] and images of ten more dots, revealing higher spatial resolution, are presented here.

III. CONTROL OF DOT DENSITY AND HEIGHT

The AFM images together with D- and H-PDFs for samples 1, 2, and 3, having $d_{\mathrm{InP}} = 7$, 4.5, and 2.9 ML, respectively, are presented in Figs. 1(a)–1(g). The D-PDFs in Figs. 1(d)–1(f) show that a reduction of d_{InP} leads to a shift of the distribution towards larger sizes (from 150 nm for sample 1 to ~200 nm for samples 2 and 3) and its broadening (from 50 nm for sample 1 to 100 nm for samples 2 and 3), which indicates elastic interaction. The H-PDF of sample 1 [Fig. 1(h)] reveals a trimodal height distribution having maxima near 5, 15, and >30 nm, denoted by A, B, and C, respectively, which was also observed in earlier studies (see [18] and references herein). The B dots also show a splitting of height at $H \sim 13$ and 21 nm, respectively. For smaller d_{InP} [Figs. 1(i) and 1(g)] C dots disappear and the height of A and B dots decreases. This leads to a reduction of the density of B dots (down to ~1 per μm^2) for sample 3. This is clearly seen in AFM images in Figs. 1(a)–1(d).

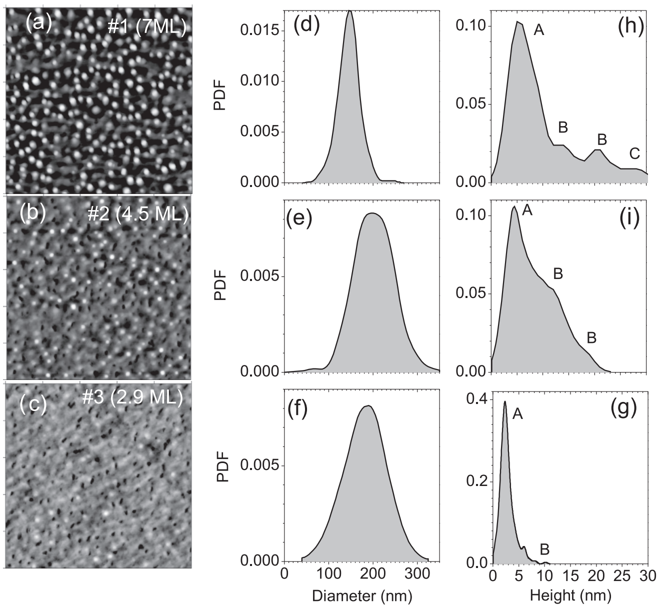

FIG. 1. Atomic force microscopy images (a–c) and probability distribution functions of dot diameter (d–f) and height (h–g) of In(Ga)P/GaInP QDs grown by deposition 7 (a, d, h), 4.5 (c, e, i), and 2.9 (c, f, g) monolayers of InP. Image size is $5 \times 5\ \mu\text{m}^{-2}$; black-white height amplitude is 80, 65, and 20 nm for (a), (b), and (c), respectively.

For sample 5 (7 ML capped) the dots A, B, and C are seen in the cross-section TEM images [Fig. 2(a)] in agreement with AFM measurements of the uncapped sample 1. The image (see also Table I) shows increase of the fraction of the B dots compared to sample 1, which indicates transformation of the A dots to the B dots due to a Ga-In interdiffusion during capping [18]. For sample 6 (3 ML capped) the Ga-In interdiffusion leads to an increase of the height of the A dots compared to uncapped sample 3 [see Figs. 2(b) and 1(g)].

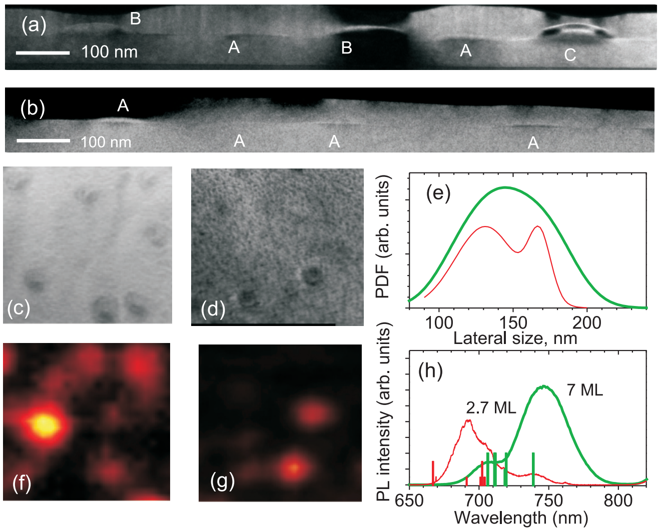

FIG. 2. Cross section (a, b) and 1×1-μm^{-2} plan view transmission electron (c, d) and near-field scanning optical (f, d) microscopy images, and size probability distribution (e) and PL spectra (h) of In(Ga)P/GaInP QD structures 5 and 6 having $d_{\text{InP}} = 7$ and 3 ML, respectively (a, c, f and b, d, g, respectively). Thick and thin curves in (e) and (h) are for $d_{\text{InP}} = 7$ and 3 ML, respectively. Low and toll bars in (h) show emission energy of single A and B dots, respectively, from Fig. 3.

Plan-view TEM images of samples 5 and 6 [Figs. 2(c) and 2(d)] show nearly the same D for both structures and a reduction of dot density for sample 6, which is naturally connected to the reduced fraction of the B dots. The same dot density reduction is also seen in the room-temperature NSOM images in Figs. 2(f) and 2(g); the appearance of a dip in D-PDF at 150 nm for sample 6 indicates the decreased fraction of the B dots.

In ensemble low-temperature μ-PL spectra in Fig. 2(h) two main bands peaked at ∼700 and 750 nm, previously assigned to the A and B dots, are seen for both structures. The relative intensity of these bands follows the increased or decreased density of the B dots. The rugged contour of the PL spectra of sample 6 is a signature of lower dot density. At the same time, a set of single dot spectra shown as bars in Fig. 2(h) and discussed below reveals B dots emitting in the region of the A band, which indicates increased Ga composition, i.e., strong Ga-In intermixing.

The data presented in Figs. 1 and 2 demonstrate control of the density and the height of In(Ga)P/GaInP QDs using variation of d_{InP}. The control of the height is important for control of WL, since for such large QDs the parabolic confinement is determined mainly by the height. In our previous study we observed a bimodal distribution of the emission linewidths (γ) of the single dots [19]. We found narrow lines ($\gamma \sim 0.5$ meV) for $\hbar\omega_0 < 3$ meV and few times broader lines ($\gamma \sim 3$ meV) for larger $\hbar\omega_0$. Thus the dots having narrow lines are B dots and demonstrate strong WL, while the dots having broader lines are A dots and demonstrate weaker WL (see below).

IV. EMISSION SPECTRUM AND NSOM IMAGING OF WIGNER MOLECULES

A. Shell structure

According to conventional selection rules for optical spectra of QDs only s-s electron-hole (e-h) transitions are allowed. These selection rules assume a low pumping power and a fast relaxation of the photoexcited carriers and are valid for the excitonic transitions in QDs having strong quantum confinement ($\hbar\omega_0 > 20$ meV) [23]. They do not account for the increased Coulomb interaction and WM formation in QDs having weak quantum confinement ($\hbar\omega_0 < 5$ meV).

In a photoexcited state of a few-electron QD the hole moves in a Hartree-Fock potential created by $N + 1$ electrons, which mixes single-particle s, p, d, … hole states. This mixing induces transitions related to occupied electronic shells for $N > 1$.

According to [24] the Coulomb interaction energy between the s hole and p and d electrons can be written as

$$E_{ss} = \frac{1}{\left(l_e^2 + l_h^2\right)^{1/2}}, \quad E_{sp} = \frac{1}{2}\frac{2l_e^2 + l_h^2}{\left(l_e^2 + l_h^2\right)^{3/2}},$$

$$E_{sd1} = \frac{1}{8}\frac{8l_e^4 + 8l_e^2 l_h^2 + 3l_h^4}{\left(l_e^2 + l_h^2\right)^{5/2}}, \text{ and } E_{sd2} = \frac{1}{4}\frac{4l_e^4 + 3l_e^2 l_h^2 + 3l_h^4}{\left(l_e^2 + l_h^2\right)^{5/2}},$$

where $l_{e,h} = \sqrt{\frac{\hbar}{m^*_{e,h}\omega_{0(e,h)}}}$ is the characteristic length of the electron and hole single-particle state; $m^*_{e,h}$ and $\omega_{0(e,h)}$ are the effective mass and confinement frequency of electron (subscript e) and hole (subscript h), respectively; and energy is expressed in units $e^2\sqrt{\pi}/4\pi\varepsilon_0\varepsilon$, where e is the charge of the electron and ε is the dielectric constant of the material.

For In(Ga)P/GaInP QDs these energies can be approximated to be $E_C \sim 0.1/l_{\text{av}}[\text{eV/nm}]$, where l_{av} is the average characteristic length of the electron and hole single-particle state in nanometers. For intermediate value of quantum confinement of our dots $\hbar\omega_0 \sim 5$ meV l_{av} is equal to ~10 nm and E_C has value ~10 meV, which is larger than $\hbar\omega_0$ and provides a strong mixing of the hole states. Thus anti-Stokes components related to occupied $p, d, \ldots$ shells of $N + 1$ electrons, residing in the QD, are activated as was observed by us in a previous study [19]. Based on this we identified QDs having zero, one, and two anti-Stokes components to QDs having $N = 1$, 2–5, and 6–9 and we further denote these dots as S, P, and D dots, respectively. The energy splitting of these emission components (for P and D dots) determines the values of $\hbar\omega_0$.

Parabolic confinement energy, $\hbar\omega_0$, determines the Wigner-Seitz radius, which is the ratio of the effective Bohr radius [25] to the distance between electrons. It is approximately equal to the ratio of Coulomb-to-kinetic energy and can be estimated as $r_s = \omega_0^{-0.5}$, where ω_0 is expressed in units of effective hartree Ha* [26]. The onset of WL is expected to occur at $r_s* \sim 2$ [19].

The mixing of the hole states suggests that the emission decay of p and d shells has the same time as that of the s shell. This is in contrast to much faster decay of these shells observed at high pumping power, generating p-p and d-d exciton transitions due to band-filling effects [27].

B. Vibronic Stokes structure

The formation of the $(N + 1)e$ WM in the photoexcited state induces Stokes components (SCs), related to c.m. and relative motion of the N electrons [19]. This can be described by a "vibronic" mechanism, similar to that of conventional molecules, and assumes a freezing of N electrons in positions of $(N + 1)e$ WM after e-h recombination.

For $N = 1$ and 2 this was shown in [19]. For $N = 1$, i.e., for S dots, the formation of $2e$ WM induces a series of the components separated by $2\hbar\omega_0$. The number ($k = 0, 1, \ldots$) and relative intensities (F_k) of these components are determined by a bond length (d_0) via Stokes shift $O = m^*_e\omega_0^2(d_0/2)^2/2\hbar\omega_0$ and Frank-Condon factors $F_k = \exp(-O) * O^k/k!$. We used values of F_k measured in PL spectra to calculate distance between electrons in the photoexcited state of S dots. According to the vibronic mechanism the emission decay of the k component is proportional to F_k.

For $N = 2$, which is a P dot in our notations, after phonon emission two electrons have azimuthal positions, which are rotated on $\Delta\phi = 30^\circ$ compared to equilibrium $2e$-WM positions. This induces SCs corresponding to rotational, $\omega_{\text{rot}} = 0.37\,\omega_0$, and odd n c.m., $n\omega_0$, modes.

Similarly, SCs related to the rotational and c.m. modes are induced for $N > 2$.

TABLE II. Parameters of electronic states of In(Ga)P/GaInP QDs measured in emission spectra.

No.[a]	$N+1$	$\hbar\omega_0$ (meV)	r_s	E_0 (eV)	Height type	x_{Ga}[b]	d_0[c] (nm)	d_{WM} (nm)	D_{NF} (nm)	D_{CD} (nm)	D[d] (nm)	$(N+1)$ e state
S1*	2	6.0	1.48	1.762	A	0				30/20	50/40	EC
S2	2	2.0	2.57	1.724	B	0.1	40	40		60/40	100/80	WM
S3	2	0.9	3.83	1.756	B	0.2	110	60	100/80	100/50	150/110	WGM
S4	2	0.6	4.69	1.743	B	0.2	140	90		110/60	170/130	WGM
S5*	2	0.5	5.13	1.859	B	0.4	80	90		110/60	170/130	WM
S6	2	9	1.21	1.781	A	0.15			20/20	20/15	40/30	EC
S7	2	2.5	2.29	1.775	B	0.15	(35)	35	60/40	50/30	90/70	WM
S8	2	5.0	1.64	1.773	A	0.15			40/20	30/20	50/40	EC
S9	2	2.0	2.57	1.712	B	0.15	40(50)	40	80/50	60/40	100/80	WM
S10	2	0.9	3.83	1.798	B	0.25	70(70)	60	110/60	100/50	150/110	WM
P1	4	5.5	1.55	1.735	A	0		30	60/60	50/40	70/60	WM
P2*	3	2.5	2.29	1.766	A	0		40		60/40	110/80	WM
P3	2	2.5	2.29	1.678	B	0.05	80	40	100/80	60/40	110/80	WM
P4	6	1.1	3.46	1.774	B	0.25	~60	45	120/90	120/90	160/130	WM
P5	3	1.0	3.63	1.744	B	0.17		80		110/70	160/130	WM
P6	6	3.5	1.94	1.715	A	0.05		40	150/130	70/60	110/90	WGM
D1	9	5.0	1.64	1.713	A	0	~20	30	60/40	60/50	90/70	WM
D2*	9	3.5	1.94	1.794	A	0		35		80/50	110/90	WM
D3*	9	3.0	2.09	1.769	B	0.2		40		90/70	130/100	WM
D4	9	1.7	2.79	1.770	B	0.2	50	50	120/100	120/90	170/140	WM
D5	7(5)	1.5(4)	2.97	1.731	A	0.1		60	20/20	130/100	170/140	WGM
D6	7-10	5.0	1.64	1.714	B	0		30	210/110	60/50	90/70	FPM

[a] Symbol * denotes 3 ML 6 structure in Table I.

[b] Estimated from dependences $E_0(x_{\text{Ga}}, H)$ and $\hbar\omega_0(D, H)$ calculated in [18].

[c] Calculated from Stokes shift (O) for S dots; measurements in NSOM images are shown in parentheses.

[d] Size of area containing 96% of electron density.

C. Charge density distributions

According to our calculations [19] made using a configuration-interaction approach described in [28,29], the number of the electrons and $\hbar\omega_0$ in QDs uniquely determines the size and spatial modulation structure of the charge density distribution.

The QDs studied have $\hbar\omega_0 \sim 0.5-9$ meV and $r_s \sim 1.5-5$ and their calculated charge density distributions show radial and azimuthal modulations, which can be related to classical WM geometries [30,31] as follows: triangle, square, pentagon, and hexagon for $N = 3$, 4, 5, and 6, respectively; hexagon and heptagon with one electron in the center, for $N = 7$ and 8, respectively; and deformed heptagon with two electrons in the center for $N = 9$. Note that, for $r_s \gg r_s*$, the classical ground-state geometry for $N = 6$ is a $\{5,1\}$ isomer, that is, a pentagon with one electron in the center [19,30,31].

Based on the analysis of our previous data [12,18,19] and accounting for a mixing of the hole states discussed above, we suggest that the spatial distribution of the emission intensity of a QD measured using NSOM corresponds to charge density distribution of $N + 1$ electrons. This neglects the effect of e-h interaction on charge density distribution. Thus, the size of NSOM image ($D_{\rm NF}$) and distance between its maxima (d_0) are equal to the size of the maxima of the charge density distribution ($D_{\rm CD}$) and the distance between its maxima ($d_{\rm WM}$).

Based on this we use measurements of $D_{\rm NF}$, d_0, and spatial arrangement of intensity maxima for direct observation of WMs and compare them to that of the charge density distribution ($D_{\rm CD}$ and $d_{\rm WM}$), calculated for particular N and $\hbar\omega_0$ values measured in the emission spectra. The values of $D_{\rm NF}$ and $D_{\rm CD}$ were used for comparison of the experiment and calculation for NSOM images measured using low spatial resolution, when d_0 cannot be measured.

V. RESULTS AND DISCUSSION

A. Specification of PL and NSOM data

Table II contains a list of the dots, the PL spectra, and NSOM images of which are presented below. The list includes ten S, six P, and six D dots. The notation (S1, S2, …, S10; P1, P2, and so on) includes the number counting the dots and symbol * indicating the structure having $d_{\rm InP} = 3$ ML (sample 6 in Table I). The table also includes the values of $N + 1$, quantum confinement ($\hbar\omega_0$), Wigner-Seitz radius (r_s), emission energy (E_0), height type (A or B), Ga content ($x_{\rm Ga}$), d_0 and $d_{\rm WM}$, and $D_{\rm NF}, D_{\rm CD}$, and D. The Ga content and dot height type have been determined using measured E_0 and $\hbar\omega_0$ values and dependences $E_0(x_{\rm Ga}, H)$ and $\hbar\omega_0(D, H)$ calculated in [18].

In Figs. 3(a)–3(e), 3(f)–3(j), and 3(k)–3(o) we show PL spectra of series of the dots S1, S2, …, S5; P1, …, P5; and D1, …, D5, respectively. The horizontal axis of the spectra is Stokes energy. Within each series $\hbar\omega_0$ changes from 6 to 0.5 meV; Wigner-Seitz radius changes from ∼1.5 to 5.13, 3.63,

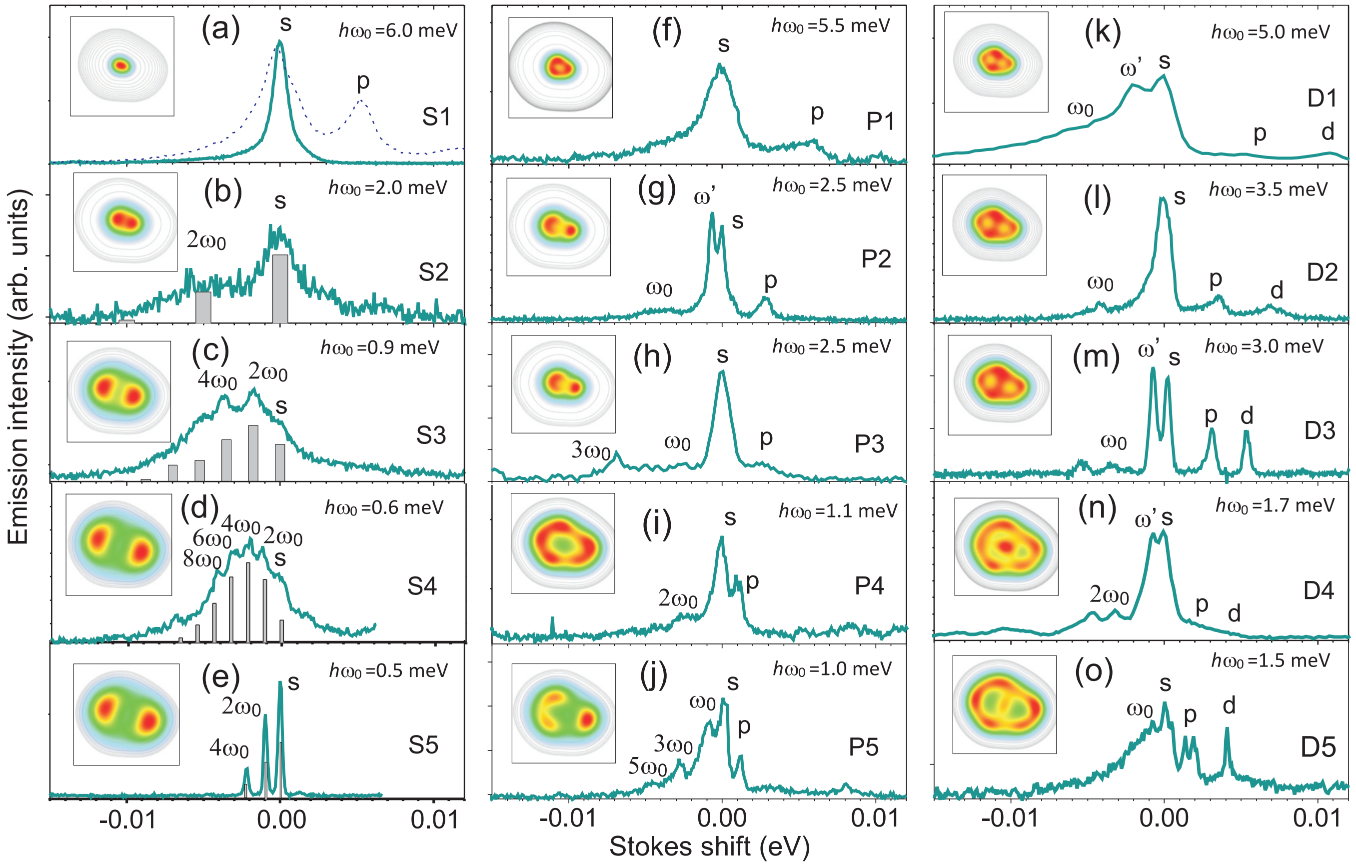

FIG. 3. Emission spectra of series of In(Ga)P/GaInP QDs having $N = 1$, 2−5, and 6−9 [(a)–(e), (f)–(j), and (k)–(o), respectively] and calculated charge density distribution (for the $N + 1$ state of these dots) in a 200×200-nm^2 frame. Dashed curves in (a) are the spectra taken at excitation power 3 mW. Bars in (a) show intensities of Stokes components calculated using the Frank-Condon model [19].

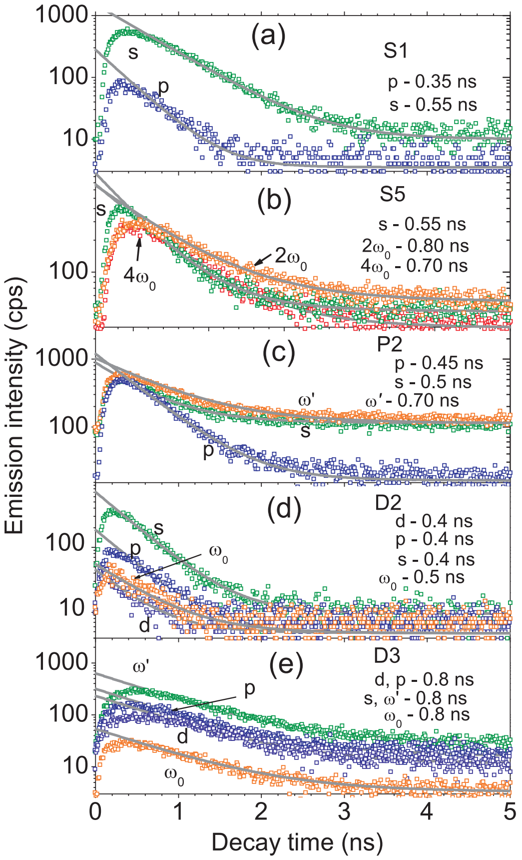

FIG. 4. Decay of emission components of S1 (a), S5 (b), P2 (c), D2 (d), and D3 (e) QDs: dots, experiment; curves, fit.

and 2.97 for S, P, and D dots, respectively. From Table II it is seen that B dots have larger r_s and thus provide stronger WL.

In Figs. 4(a)–4(e) we show measured emission intensity of the spectral components for dots S1, S5, P2, D2, and D3 versus time, i.e., decay curves. In the figure we also present fitting curves and values of the emission decay time τ_0 for each spectral component obtained from the fitting.

The NSOM images of *s* peak of P4, D4, D1, and D5 dots are presented in Figs. 5(d)–5(g) and those of S3, P1, and P4 dots are presented in [19]. In Fig. 5 we also show spectra and NSOM images of a few other dots. These are S6–S10 [Figs. 5(a)–5(c)], P6 [Fig. 5(h)], and D6 [Fig. 5(i)] dots. The spectra of the dots S6, S7, and S8 presented in Fig. 5(a) overlapped strongly and were separated using Lorentzian contour decomposition. The NSOM images of these dots were measured during single scan using detection energy and width 1.78 and 0.005 eV, respectively.

The calculated charge density distributions are shown in the insets of Figs. 3(a)–3(o) and Figs. 5(a)–5(i).

More detailed data on NSOM imaging of the dot D5 and NSOM image of dot D7, which is similar to the D6 dot, are presented in Supplemental Material [32].

B. Wigner localization

1. Excitonic dots

The PL spectra of the dots S1, S6, and S8 [see Figs. 3(a) and 5(a)] show a single line, resulting from a singly charged 2*e*-*h* excitonic complex (EC) trion. The dots have $\hbar\omega_0 = 5{-}9$ meV and $r_s \sim 1.5$ near the upper limit of quantum confinement and lower limit of Wigner-Seitz radius measured. The emission area estimated from NSOM in Fig. 5(a) has size $D_{\rm NF}$, 20×20 and $40 \times 20\,{\rm nm}^2$ for the dots S6 and S8, respectively, in agreement with the calculations (see Table II).

2. S dots

The spectra of the dots S2, S3, S4, and S5 in Figs. 4(b)–4(e) and S9 and S10 in Figs. 5(b) and 5(c), having $\hbar\omega_0 = 0.5{-}2$ meV, show vibronic SCs, indicating decomposition of the trion and formation of the 2*e*-*h*-WM complex. The decomposition occurs at $r_s > r_s^*$ and results in formation of an *e* dimer, seen in charge density distributions in Figs. 3(b)–3(e).

The Stokes shift values obtained for S2, S3, S4, and S5 dots are $O = 0.5$, 1.5, 2.5, and 0.7, respectively, which correspond to $d_0 = 40$, 110, 140, and 90 nm. The S9 and S10 dots have $O = 0.5$ and 0.9 and $d_0 = 40$ and 70 nm. Note that dots S2 and S9, both of which have $\hbar\omega_0 = 2$ meV, have the same O and d_0, while dots S3 and S10, both of which have $\hbar\omega_0 = 0.9$ meV, have different O and d_0.

The dots S2, S5, S9, and S10 have $F_1 < F_0$ and their d_0 value is very close to a calculated bond length of a 2*e* WM, $d_{\rm WM}$, (see Table II). Moreover NSOM images of S9 and S10 dots in Figs. 5(b) and 5(c) reveal corresponding 2*e*-WM patterns, providing direct measurements of WM formation. This confirms the vibronic approach and NSOM imaging mechanism discussed above. Also the NSOM image of S7 in Fig. 5(a) shows the 2*e*-WM pattern having $d_0 = 30$ nm, which corresponds to $\hbar\omega_0 = 2.5$ meV and $r_s = 2.29$. For this dot d_0 cannot be estimated using measurements of F_k, since their Stokes components strongly overlapped with emission lines of S6 and S8 dots [Fig. 5(a)]. The larger emission intensity observed for the left NSOM image maxima in the S9 dot indicates spatial inhomogeneity of *e*-*h* excitation or relaxation.

3. Photoexcited state of P and D dots

Formation of $(N+1)e$ WMs in the photoexcited state in P and D dots is evident from the calculated charge density distributions in Figs. 3(f)–3(o) and Figs. 5(d)–5(i) and is confirmed in NSOM imaging experiments for P4, D4, and D1 dots [see NSOM images in Figs. 5(d), 5(e), and 5(f), respectively] and for P1 and P3 dots [see NSOM images in [19]).

For P4 and D4 QDs [Figs. 5(d) and 5(e), respectively] the NSOM images, i.e., their spatial modulation and distance between maxima, are in a very good agreement with that of the calculated charge density distributions (see Table II), and thus the NSOM measurements presented are a direct observation of 6*e* and 9*e* WMs. The images, however, show much larger differences in the intensity of the maxima than the charge density, which appear as stronger intensity of left and central maxima of the images of P4 and D4 dots, and which, probably, indicate spatial inhomogeneity of *e*-*h* excitation or relaxation. While at these r_s (~ 3) individual electrons are not fully separated and the number of the charge density maxima is smaller than the number of electrons, the observed images show correspondence to classical {6,0} and {7,2} isomers.

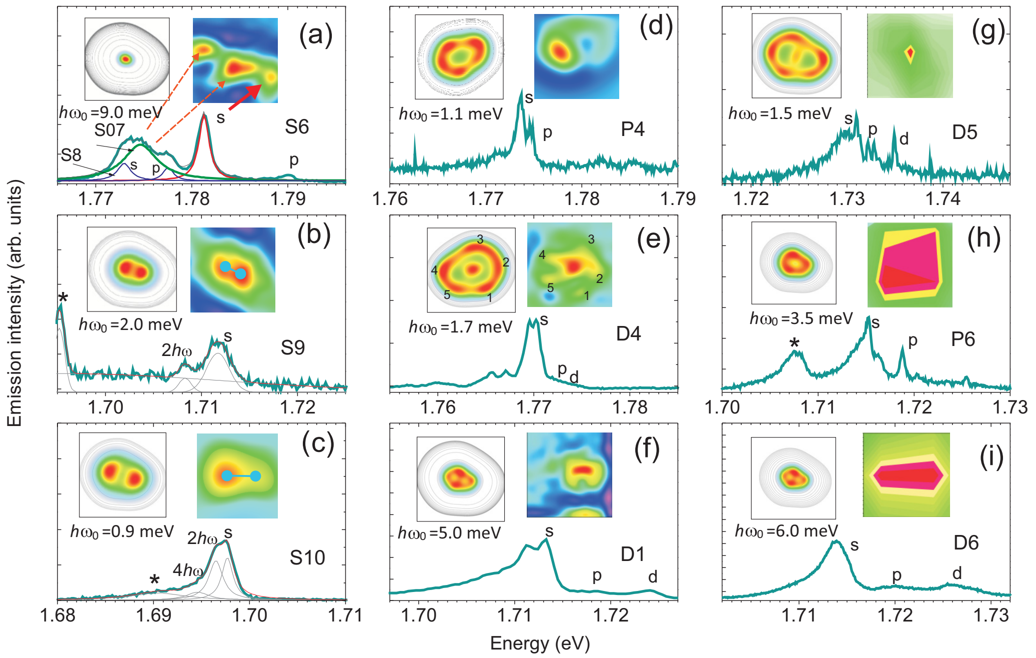

FIG. 5. NSOM images (right insets) and charge density distribution (left insets) (size $200 \times 200\,\mathrm{nm}^2$) and emission spectra of nine In(Ga)P/GaInP QDs. For spectra (a), (b), and (c) a Lorentzian contour decomposition is shown. Dumbbells in (b) and (c) outline electron separation measured from SC intensity distribution. The stars denote neighboring dots.

For P3 having $r_s = 2.29$ the triangle shape image gives $N + 1 = 3$ [19]. However, the measured d_{WM} is nearly two times larger than the calculated one. This can indicate clustering of electrons or formation of WGMs and needs more detailed investigations.

For dots P1 [19] and D1 [Fig. 5(f)] having $r_s = 1.55$ and 1.64, respectively, formation of the WM having $N + 1 = 4$ and 7, respectively, is evident from good agreement between D_{NF} and D_{CD} values. Note that for dots P1 and D1, which have $r_s < r_s^*$, charge density distributions reveal molecular-type modulations similar to the dots having larger r_s.

4. *Ground state of P and D dots*

The SC structure, manifesting formation of the *Ne* WM in the ground state, was observed for all the dots having $r_s > r_s^*$.

The dots P2, P3, and P5 in Figs. 3(g), 3(h), and 3(j), having $r_s = 2.29$, 2.29, and 3.63 reveal SCs of 2*e* WM. Thus the peak denoted ω' observed for the P2 dot can be assigned to the rotational mode. For dots P3 and P5 this mode is not observed, which can be due to its weak intensity and d_0 anomaly (in P3) and small frequency (in P5). An odd $n\omega_0$ series is strong in P5 having $r_s = 3.63$ and is suppressed for smaller r_s dots, P2 and P3, as can be expected. The difference in SC intensity distributions of these dots can be related to the d_0 anomaly of dot P3.

For $N > 2$ the c.m. ω_0 and $2\omega_0$ peaks are seen in the dots D1, D2, D3, and D5 and P4 and D4, respectively, and the rotational ω' peak is seen in the dots D1, D3, and D4.

The spectra of the dots D1 and D4 having $N = 8$ [see Figs. 3(k) and 3(n), respectively] reveal the same number of spectral components having the same intensity distribution, which demonstrate scaling of WM emission spectra structure with r_s in the range 1.64–2.79. The increase of r_s is accompanied by narrowing of the emission components, similar to that observed for S dots [19] [see also Figs. 3(b)–3(e), 5(b), and 5(c)]. Both show strong rotational and weak c.m. components and the only difference seen in the spectra is a suppression or activation of ω_0 and $2\omega_0$ components in D1.

The $2\omega_0$ component is also observed for 5*e* WMs P4 dots and this observation needs further analysis.

The dots D2 [Fig. 3(l)] and D3 [Fig. 3(m)] having $r_s = 1.94$ and 2.09 reveal nearly the same spectral components as dots D1 and D4, and thus can be assigned to the 8*e* WMs. Having only small difference in $r_s \sim r_s^*$, however, they show quite different spectral width (γ) and decay of the emission components (see below). D3 also has a strong ω' component, which is not seen in dot D2, which can manifest different electron arrangement.

5. *Decay of the emission components*

Time-resolved measurements of the dots P2, D2, and D3 presented in Figs. 4(c), 4(d), and 4(e) show that the emission decay time τ_0 of their *p* and *d* components has the same value as the decay time of the *s* component (0.5, 0.4, and 0.8 ns, respectively), which is a signature of strong Coulomb interaction and mixed hole state. This is different than the S1 QD, in which the *p* peak in Fig. 3(a) is observed only at high pumping power, and it has nearly two times faster emission decay [0.35 versus 0.5 ns in Fig. 4(a)].

Time-resolved measurements also show that SCs have longer τ_0 than the *s* peak [see data for $2\omega_0$ and $4\omega_0$ peaks of the S5 dot in Fig. 4(b) and for the ω' peak of the P2 dot in in Fig. 4(c)], which reflects their vibronic nature.

The dot D3 shows two times larger τ_0 compared to D2 [Figs. 4(d) and 4(e)], which is accompanied by three times smaller γ. The narrow width of the emission components in D3 is similar to WGM dots discussed below. At the same

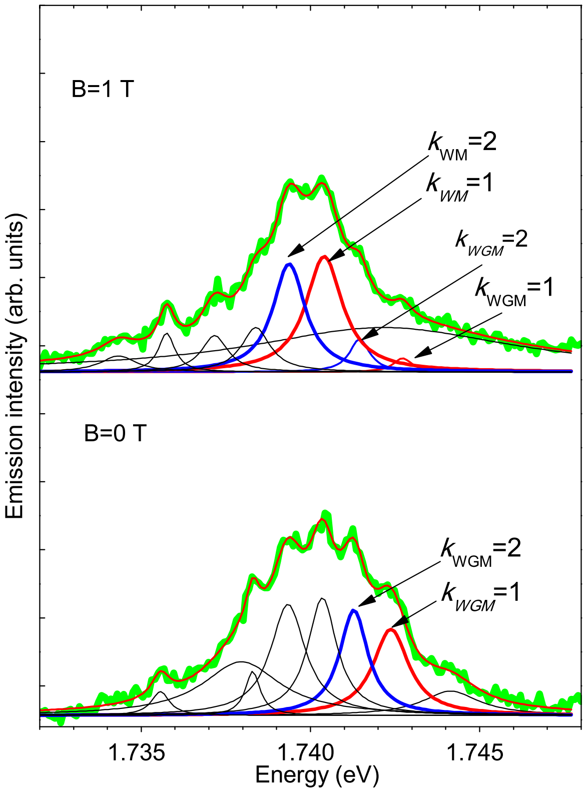

FIG. 6. Emission spectrum of the S4 dot and its Lorentzian contour decomposition measured at magnetic field 0 and 1 T.

time Stokes components for both dots show the same τ_0 as the *s* component, which indicates a mixed hole rather than a vibronic state.

C. Cavity effects

1. S dots

In contrast to S2, S5, S9, and S10 dots discussed above and having $F_1 < F_0$, the dots S3 and S4 have $F_1 > F_0$ indicating that $d_0 > d_{\mathrm{WM}}$. We found for these dots $d_0 \sim 2d_{\mathrm{WM}}$, which is very close to a calculated size of charge distribution, i.e., to the dot size D (see Table II). Also d_0 for S3 is close to the size of the emission area D_{NF} measured. This shows that the photoexcited state of these dots is a WGM formed due to a hard-wall edge potential. For these dots a ground-state energy of $2e$ WM is $E \sim 3$ meV and they have kinetic and Coulomb energy contributions of 1 and 2 meV, respectively [12]. Thus the resonant cavity mode has energy $E_{\mathrm{cav}} \sim 1.5 \pm 0.5$ meV and de Brogile wavelength $\lambda_{\mathrm{cav}} \sim 70 \pm 30$ nm [33]. For the dot diameter $D \sim 130$ nm the resonant mode is $\mathrm{WGM}_{6,1}$ having azimuthal and radial number 6 and 1, respectively.

We can expect that magnetic field will suppress a propagation of WGM, when the size of a cyclotron orbit, D_{cycl}, becomes smaller than D. In Fig. 6 we show the emission spectra of the dot S4 at magnetic fields $B = 0$ and 1 T. One can see that the intensity distribution of SCs at $B = 1$ T is quite different compared to $B = 0$ T and has a condition $F_1 < F_0$. This manifests a suppression of WGM and formation of WM. Since the condition $D_{\mathrm{cycl}} \sim D$ for this dot occurs at $B_s \sim 0.5$ T [34], this observation confirms formation of the $2e$ WGM cavity. Formation of the WGM can explain unusual dependence of SC shifts in magnetic field for this dot observed [19]. We should point out that similar behavior was observed for another WGM S dot, the data for which will be published elsewhere.

While, in general, formation of WGMs in a $2e$ QD can be expected at relatively small $D < 50$ nm and $r_s < r_s^*$ [12], we observed them for $D \sim 150$ nm and $r_s \sim 4$, which indicates the important role of the Coulomb interaction. Also the WGM was observed in dots (S3 and S4) having emission energy E_0 near 1.75 eV and Ga composition ~0.2. At the same time a WGM was not observed in dots S5 and S10 having the same D but larger emission energy (>1.8 eV) and Ga content (>0.25). This can indicate important role of Ga fluctuations at the dot edge on the formation of the WGMs.

2. P and D dots

While for P1–P5 and D1–D4 QDs discussed above, the NSOM images show good agreement with calculated charge distributions, the dots D5, P6, and D6 [see Figs. 5(f), 5(h), and 5(i), respectively] reveal drastic difference in D_{NF} and D_{CD}: D_{NF} is a few times smaller than D_{CD} for the dot D5 and a few times larger for the dots P6 and D6.

For the dot D5 we analyzed the NSOM images of all spectral components observed (see Supplemental Material [32]), which allows us to establish the WGM nature of the *p* peak and suggest that $N + 1 = 5$, $\hbar\omega_0 = 4.5$ meV, and $D \sim 80$ nm for this dot (see Table II). Thus the cavity mode observed is $\mathrm{WGM}_{10,1}$. This analysis will be published elsewhere.

For dot P6 $D_{\mathrm{NF}} \sim 2D_{\mathrm{CD}}$ and is consistent with similar findings made for the other P-type dot [19] and the fact that $D_{\mathrm{NF}} > D$ can indicate interference between WM and WGM states, or the effect of magnetic field generated by a WGM [12]. On the other hand its quantum confinement, emission energy, Ga content, and spectrum structure are very similar to that of dot D5, which indicates the conditions for WGM formation in P dots (i.e., $D \sim 100$ nm, $\hbar\omega_0 \sim 4$ meV, $N = 4$, $x_{\mathrm{Ga}} \sim 0.05$).

For dot D6 the NSOM image shows an elongated shape, which suggests the Fabry-Perot mode (FPM), and the fact that $D_{\mathrm{NF}} \sim 2D$ indicates $N \sim 10$. We observed a similar elongated image for another dot, having similar emission spectra (see Supplemental Material [32]). Note that the appearance of *e* FPMs together with *e* WGMs can be expected for QDs, which are electron analogs of photon microdisk cavities, for which the coexistence of the quantum confined modes, WGMs and FPMs, is well established [35].

VI. CONCLUSIONS

We used structural AFM and TEM measurements to demonstrate our control of the density and size distribution of MOVPE-grown In(Ga)P/GaInP quantum dots using variation the InP thickness from 2 to 7 ML. These QD structures could represent natural electronic Wigner molecule systems, as well as natural electron cavities for WGMs. Using optical PL and NSOM measurements of these structures we investigated the dependence of the emission spectra of single dots on the number of electrons present and the extent of quantum confinement, using a set of nearly 120 individual QDs. We provided a detailed analysis of the spectral, spatial, and temporal distribution of the emission intensity of a subset of these dots having $N = 1$–9 (present by means of background doping) and quantum confinement in the range $\hbar\omega_0 = 0.5$–6 meV. We also present the analysis of the effect of Wigner localization on the emission properties and NSOM imaging of strongly correlated electrons in QDs and the calculations of charged density distributions. In most of the cases, the calculations agree closely with the experimental results. From this analysis we demonstrated the formation of $2e$, $3e$, $6e$, and $9e$ Wigner molecules and $2e$, $4e$, and $7e$ WGMs and e FPMs of these QDs. These results provide direct experimental evidence for the clear observations of Wigner molecule formation and existence of electron WGMs in these QDs as well as FPMs. We have also demonstrated the unique capabilities of high-spatial-resolution photoluminescence (i.e., NSOM) for the characterization of quantum systems having strong electron correlation. These techniques can be critical for the development of the application of these structures for novel quantum devices and for quantum computing.

ACKNOWLEDGMENTS

A.M.M. and D.V.L. acknowledge support from the Ministry of Education and Science of the Russian Federation (Contract No. 14.Z50.31.0021). K.G.B., M.V.R., and A.A.T. acknowledge the financial support of the Russian Science Foundation (Project No. 14-22-00107).

[1] L. P. Kouwenhoven, D. G. Austing, and S. Tarucha, Rep. Prog. Phys. **64**, 701 (2001).

[2] R. Hanson, L. P. Kouwenhoven, J. R. Petta, S. Tarucha, and L. M. K. Vandersypen, Rev. Mod. Phys. **79**, 1217 (2007).

[3] C. Ellenberger, T. Ihn, C. Yannouleas, U. Landman, K. Ensslin, D. Driscoll, and A. C. Gossard, Phys. Rev. Lett. **96**, 126806 (2006).

[4] S. Kalliakos, M. Rontani, V. Pellegrini, C. P. Garcia, A. Pinzuk, G. Goldoni, E. Molinari, L. N. Pfeiffer, and K. W. West, Nat. Phys. **4**, 467 (2008).

[5] A. Singha, V. Pellegrini, A. Pinczuk, L. N. Pfeiffer, K. W. West, and M. Rontani, Phys. Rev. Lett. **104**, 246802 (2010).

[6] A. Gamucci, V. Pellegrini, A. Singha, A. Pinczuk, L. N. Pfeiffer, K. W. West, and M. Rontani, Phys. Rev. B **85**, 033307 (2012).

[7] P. A. Maksym, H. Imamura, G. P. Mallon, H. Aoki, J. Phys.: Condens. Matter **12**, R299 (2000).

[8] S. M. Reimann and M. Manninen, Rev. Mod. Phys. **74**, 1283 (2002).

[9] B. Szafran, S. Bednarek, and J. Adamowski, J. Phys.: Condens. Matter **15**, 4189 (2003).

[10] C. Yannouleas and U. Landman, Phys. Rev. B **84**, 165327 (2011).

[11] C. Nayak, S. H. Simon, A. Stern, M. Freedman, and S. D. Sarma, Rev. Mod. Phys. **80**, 1083 (2006); S. D. Sarma1, M. Freedman, and C. Nayak, npj Quantum Information **1**, 15001 (2015).

[12] A. M. Mintairov, J. L. Merz, J. Kapaldo, A. S. Vlasov, and S. A. Blundell, Semiconductors **52**, 502 (2018).

[13] G. Reecht, H. Bulou, F. Scheurer, V. Speisser, B. Carrière, F. Mathevet, and G. Schull, Phys. Rev. Lett. **110**, 056802 (2013).

[14] Y. Zhao, J. Wyrick, F. D. Natterer, J. F. Rodriguez-Nieva, C. Lewandowski, K. Watanabe, T. Taniguchi, L. S. Levitov, N. B. Zhitenev, and J. A. Stroscio, Science **348**, 672 (2015).

[15] S. Ilani, J. Martin, E. Teitelbaum, J. H. Smet, D. Mahalu, V. Umansky, and A. Yacoby, Nature (London) **427**, 328 (2004).

[16] S. Kalliakos, C. P. García, V. Pellegrini, M. Zamfirescu, L. Cavigli, M. Gurioli, A. Vinattieri A. Pinczuk, B. S. Dennis, L. N. Pfeiffer, and K. W. West, Appl. Phys. Lett. **90**, 181902 (2007).

[17] M. Ciorga, A. S. Sachrajda, P. Hawrylak, C. Gould, P. Zawadzki, S. Jullian, Y. Feng, and Z. Wasilewski, Phys. Rev. B **61**, R16315 (2000).

[18] J Kapaldo, S. Rouvimov, J. L. Merz, S. Oktyabrsky, S. A. Blundell, N. Bert, P. Brunkov, N. A. Kalyuzhnyy, S. A. Mintairov, S. Nekrasov, R. Saly, A. S. Vlasov, and A. M. Mintairov, J. Phys. D **49**, 475301 (2016).

[19] A. M. Mintairov, J. Kapaldo, J. L. Merz, A. S. Vlasov, and S. A. Blundell, Phys. Rev. B **95**, 115442 (2017).

[20] A. V. Shelaev, A. M. Mintairov, P. S. Dorozhkin, and V. A. Bykov, J. Phys.: Conf. Ser. **741**, 012132 (2016).

[21] M. V. Rakhlin, K. G. Belyaev, I. V. Sedova, S. V. Sorokin, S. V. Gronin, A. A. Usikova, A. A. Sitnikova, P. N. Brunkov, S. V. Ivanov, and A. A. Toropov, Phys. Status Solidi C **13**, 514 (2016).

[22] A. M.Mintairov, K. Sun, J. L. Merz, C. Li, A. S. Vlasov, D. A. Vinokurov, O. V. Kovalenkov, V. Tokranov, and S. Oktyabrsky, Phys. Rev. B **69**, 155306 (2004).

[23] A. Wojs and P. Hawrylak, Phys. Rev. B **55**, 13066 (1997).

[24] R. J. Warburton, B. T. Miller, C.S. Dürr, C. Bödefeld, K. Karrai, J.P. Kotthaus, G. Medeiros-Ribeiro, P. M. Petroff, and S. Huant, Phys. Rev. B **58**, 16221 (1998).

[25] In effective atomic units Bohr radius $a_B^* = \hbar^2(4\pi\varepsilon\varepsilon_0)/m^*e^2$, where ε and m^* are the dielectric constant of the material and effective mass of the electron, respectively. For our dots it is 8.7 nm.

[26] In effective atomic units $\mathrm{Ha}^* = 2\mathrm{Ry}^*$, where Rydberg $\mathrm{Ry}^* = m^*e^4/2\hbar^2(4\pi\varepsilon\varepsilon_0)^2$. For our dots it is 13.2 meV.

[27] E. Dekel, D. V. Regelman, D. Gershoni, and E. Ehrenfreund, W. V. Schoenfeld, and P. M. Petroff, Phys. Rev. B **62**, 11038 (2000).

[28] S. A. Blundell and K. Joshi, Phys. Rev. B **81**, 115323 (2010).

[29] S. A. Blundell and S. Chacko, Phys. Rev. B **81**, 121104(R) (2010); **83**, 195444 (2011).

[30] F. Bolton and U. Rossler, Superlattices Microstruct. **13**, 139 (1993).

[31] M. Saint Jean, C. Even, and C. Guthmann, Europhys. Lett. **55**, 45 (2001).

[32] See Supplemental Material at http://link.aps.org/supplemental/10.1103/PhysRevB.97.195443 for additional NSOM imaging data.

[33] $\lambda_{dB} = \hbar/\sqrt{2m^*E}$, where $m^* = 0.08m_0$ is the electron effective mass in the In(Ga)P QD and m_0 is the mass of the free electron.

[34] $D_{\mathrm{cycl}} = 2v/\omega_c$, $v_{\mathrm{cav}} = (2E_{\mathrm{cav}}/m^*)^{0.5}$ is Fermi velocity, and $\omega_c = eB/m^*$ is cyclotron angular frequency. For $E_{\mathrm{cav}} = 1.5$ meV $v_{\mathrm{cav}} = 7.4 \times 10^4$ m/s and $D_{\mathrm{cycl}}B \sim 70$ nm T.

[35] A. M. Mintairov, Y. Chu, Y. He, S. Blokhin, A. Nadtochy, M. Maximov, V. Tokranov, S. Oktyabrsky, and J. L. Merz, Phys. Rev. B **77**, 195322 (2008).